PHOTONICS

Multimodality integrated microresonators using the Moiré speedup effect

Qing-Xin Ji[1]†, Peng Liu[1]†, Warren Jin[2,3]†, Joel Guo[2], Lue Wu[1], Zhiquan Yuan[1], Jonathan Peters[2], Avi Feshali[3], Mario Paniccia[3], John E. Bowers[2]*, Kerry J. Vahala[1]*

High-*Q* microresonators are indispensable components of photonic integrated circuits and offer several useful operational modes. However, these modes cannot be reconfigured after fabrication because they are fixed by the resonator's physical geometry. In this work, we propose a Moiré speedup dispersion tuning method that enables a microresonator device to operate in any of three modes. Electrical tuning of Vernier coupled rings switches operating modality to Brillouin laser, bright microcomb, and dark microcomb operation on demand using the same hybrid-integrated device. Brillouin phase matching and microcomb operation across the telecom C-band is demonstrated. Likewise, by using a single-pump wavelength, the operating mode can be switched. As a result, one universal design can be applied across a range of applications. The device brings flexible mixed-mode operation to integrated photonic circuits.

The Vernier effect, which is used in measurement instruments such as calipers and micrometers, overlays two scales or rulings with slightly different divisions to improve accuracy. Its analog in optical resonators overlays two frequency scales with different divisions set by the free spectral range, *FSR*, of two resonators. The coupling of such resonators is mediated by the frequency Vernier and creates useful tuning effects that benefit optical add-drop filters (*1*), semiconductor lasers (*2*), and frequency microcombs (*3*–*8*). Verniers feature a larger scale periodicity that is associated with the Moiré pattern (*9*) that they form when overlaid. This Moiré pattern exhibits a speedup effect when either scale in the Vernier is shifted. That is, when the two sets of scales are displaced differentially, the collective movement of the Moiré pattern is multiplied by the Vernier ratio (*R*) (*9*, *10*). In this work, the speedup effect is adapted to demonstrate broadband electrical control (through differential thermal tuning) of dispersion.

Generally, anomalous dispersion is necessary for mode locking of bright-soliton microcombs (*11*), which feature a femtosecond timescale optical pulse and have applications in various fields such as light detection and ranging (LIDAR) (*12*, *13*), dual-comb spectroscopy (*14*, *15*), optical frequency synthesis (*16*), optical clocks (*17*), and astrocombs (*18*, *19*). Conversely, although they have narrower spectral coverage compared with bright microcombs, normal dispersion microcombs (*20*) offer higher power efficiency and comb line power. These properties are advantageous for applications such as microwave generation through photodetection (*21*) and wavelength division multiplexing (WDM)–based coherent optical communications (*22*, *23*). Finally, Brillouin lasers are known for their high spectral coherence (*24*, *25*), which is useful in applications that include microwave signal generation (*26*), gyroscopes (*27*), and clock signal sources (*28*). However, they require precise phase matching for operation, and this involves setting the frequency difference between two optical resonances to closely match the phonon frequency shift. The phase-matching condition is normally set during device fabrication by adjusting the device *FSR* (i.e., device diameter). In effect, this permanently fixes the pump wavelength (i.e., each device has a set pumping wavelength). As now shown, on-demand operation across the C-band is possible for each of these three modes of operation.

Results

Our prototype device consists of a pair of coupled, single-mode Si_3N_4 racetrack-shaped ring resonators with metallic heaters deposited along their periphery and wire bonded to a printed circuit board for electrical control (Fig. 1, A to C). Further device details are provided in the supplementary materials, but briefly, the intrinsic *Q* factor is 95 million, the average *FSR* of the two rings is 19.95 GHz, and their *FSR* difference δFSR is 100 MHz, so that $R \approx FSR/\delta FSR = 200$. The rings couple along a straight section to form hybrid-mode frequency bands (*7*, *8*) whose dispersion spectra are modulated by the Moiré effect. By applying voltage to one of the ring heaters, the frequency ruling of the corresponding resonator is shifted, thereby inducing a much larger spectral shift of the dispersion through the speedup effect. Large changes in dispersion over frequency spans in excess of the telecom C-band are possible, so that a single device can be reconfigured on demand operation in several different modalities.

To illustrate this concept, Fig. 1, D to F, shows, respectively, the spectra from a single device operated as a stimulated Brillouin laser (SBL), a bright-pulse microcomb, and a dark-pulse microcomb. Each of these operational modes was set by differential tuning of the resonators. Electrical spectra of the beatnote between the pump laser and SBL, as well as the photodetected outputs of the microcombs are shown in the insets. Moreover, on account of the high optical *Q* of the coupled rings, and the correspondingly low turn-on power of these devices, direct pumping from the same semiconductor laser is possible in a hybrid-integrated design (see Fig. 1B).

The Moiré speedup effect is depicted in Fig. 2A, where the mode frequencies within two resonators (rings A and B) are depicted as black lines. The line spacings, which correspond to the *FSR*s, are assumed to be slightly different, and their initial Moiré pattern is illustrated by light red shading. As a result of modal coupling between the two rings, the Moiré pattern dictates the mode hybridization and, consequently, the dispersion characteristics. Lighter regions in the Moiré pattern indicate that ring-mode frequencies coincide to form antisymmetric and symmetric hybrid modes. On the other hand, in the "interleaved" regions where the mode resonant frequencies are spaced by *FSR*/2, the mode hybridization is greatly reduced (circled dots in Fig. 2A). Next, we assume that the modes in ring B are tuned by an optical frequency Δf_{diff} relative to the modes in ring A. The minute adjustment is magnified by the Vernier ratio *R*, causing a large shift in the Moiré pattern by Δf_{o} ($\Delta f_{\mathrm{o}} = R\Delta f_{\mathrm{diff}}$) that is illustrated by the blue-shaded region.

The integrated dispersion of the coupled-ring system is measured using a calibrated Mach-Zehnder interferometer (*29*) and is shown for the two hybridized frequency bands in Fig. 2B. Here, the quantity plotted is the integrated dispersion, which is defined by $D_{\mathrm{int,c}} = \omega_\mu - \omega_{\mathrm{o}} - \bar{D}_1\mu - \frac{1}{2}D_{2,\mathrm{o}}\mu^2$, where $\omega_{\mathrm{o}}/2\pi$ is mode resonance frequency at relative mode number $\mu \equiv m - m_{\mathrm{o}} = 0$, where *m* is the actual mode number and m_{o} corresponds to the mode number at 1550 nm. Also, $\bar{D}_1/2\pi$ is the average *FSR* of the two rings, and $D_{2,\mathrm{o}}$ is the waveguide intrinsic group velocity dispersion (see supplementary materials for details). By differential tuning of the ring *FSR*s, the second set of dispersion spectra are measured in Fig. 2B. Overall, the dispersion curve is shifted by 2.0 THz, with an estimated temperature difference of 6°C that corresponds to a frequency shift of 10 GHz. Also presented in the figure are curves from a dispersion model that is described in the supplementary materials.

In Fig. 2C, dispersion spectra of the upper and lower frequency bands are again measured,

[1]T. J. Watson Laboratory of Applied Physics, Caltech, Pasadena, CA 91125, USA. [2]ECE Department, University of California, Santa Barbara, Santa Barbara, CA 93106, USA. [3]Anello Photonics, Santa Clara, CA 95054, USA.
*Corresponding author. Email: jbowers@ucsb.edu (J.E.B.); vahala@caltech.edu (K.J.V.)
†These authors contributed equally to this work.

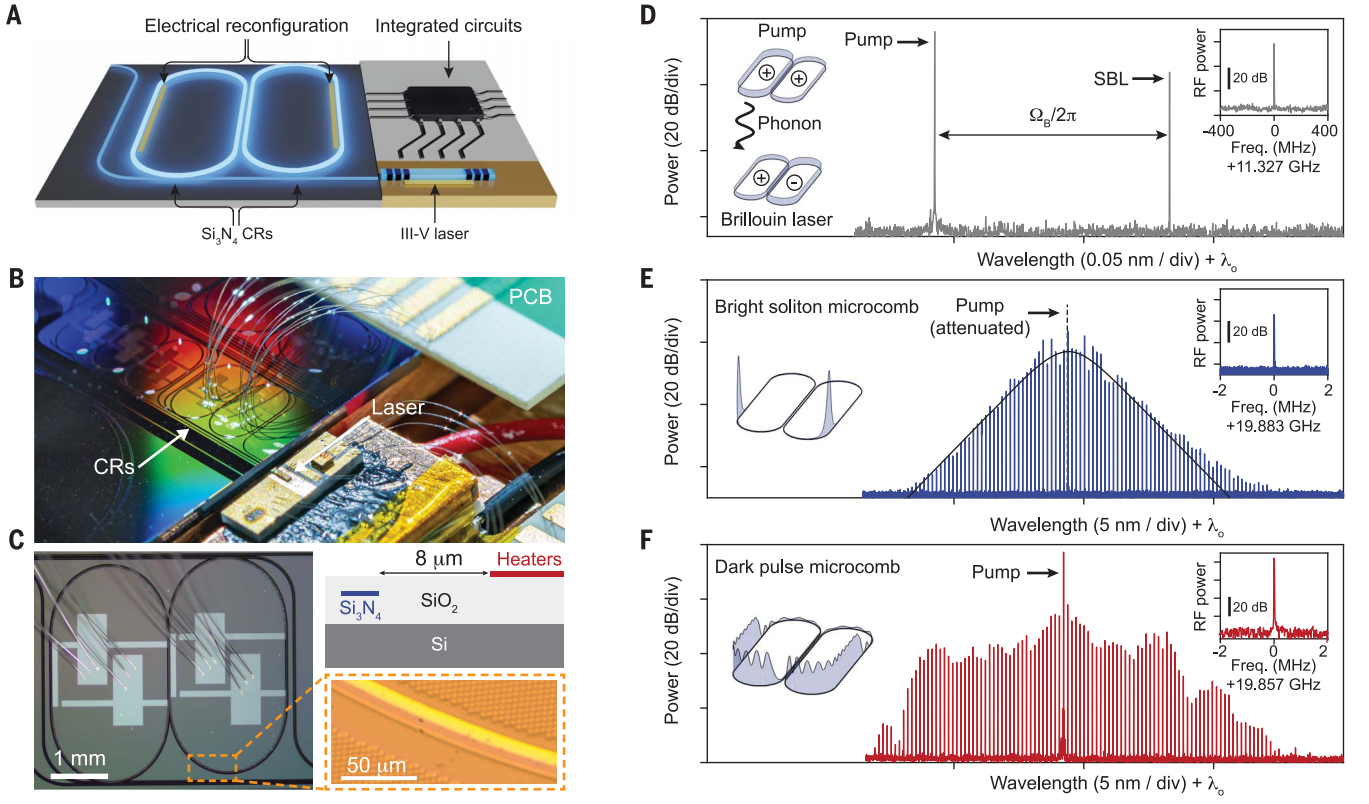

Fig. 1. A hybrid-integrated microresonator and optical pump can be operated as a Brillouin laser, bright microcomb, or dark-pulse microcomb source with on-demand electrical control and at a user-defined wavelength across the C-band. (**A**) Illustration of the reconfigurable hybrid-integrated device. Si_3N_4 coupled rings (CRs) are directly pumped by an integrated III-V laser. Dispersion of the CRs is tuned by differential tuning of the rings with integrated resistive heaters. The III-V laser and the heaters are wire bonded to printed circuit boards (PCBs) for electrical control. (**B**) Photograph of the integrated device depicted in (A). (**C**) Zoomed-in image of the coupled racetrack ring resonator. Resistive heaters are deposited atop the chip and offset from the Si_3N_4 waveguide by 8 μm to avoid metal-induced optical absorption. (**D** to **F**) Optical spectra for on-demand operation of the Brillouin laser (D), bright microcomb (E), and dark-pulse microcomb (F), all operated at the same III-V laser pumping wavelength λ_o = 1548.4 nm per the system layout in (B). In each case, dispersion is reconfigured through simple electrical tuning. In (E), the black curve denotes the $sech^2$ envelope and gives an optical pulse width of 800 fs. Insets on the left are schematic drawings of Brillouin emission between symmetric and antisymmetric hybrid modes (D) and pulse shape temporal waveforms inside the coupled rings [(E) and (F)]. Insets on the right show radio frequency (RF) beatnote (D) between the pump laser and Brillouin laser (resolution bandwidth is 100 kHz) and repetition rate tone [(E) and (F)], confirming mode locking (resolution bandwidth is 10 kHz). div, division; $\Omega_B/2\pi$, Brillouin frequency shift.

except for common-mode (not differential) tuning of the two rings. There is no measurable change in dispersion under this common-mode tuning (note that the red and blue spectra are shifted vertically for comparison). Finally, to obtain an approximate value for the applied differential temperature change for the measurements in Fig. 2B, common-mode frequency tuning data (inset of Fig. 2D) are used to infer differential temperature change, as shown in Fig. 2D. Here, the measured dispersion shift at three points in Fig. 2A is first plotted versus frequency by assuming a theoretical R = 200 (expressed as 0.2 THz/GHz in the figure). Then, this scale is converted to differential temperature (upper horizontal axis) by using the common-mode tuning data (Fig. 2D, inset data). By comparing the electrical power consumption of the heaters, the measured differential tuning efficiency is 19.2 GHz/W, which corresponds to a phase change of 6.2×10^{-4}/W.

Besides operation of a single device in three different modalities (see Fig. 1, D to F), it is important to note that operation wavelength in any of these modes can be broadly tuned to match the requirements of a specific pump laser. For example, pumping of the upper band in Fig. 2B will induce stimulated Brillouin lasing in the lower band, provided that the difference in these frequencies ($\Delta\omega$) matches the phonon frequency. This idea is illustrated in Fig. 3A, which plots $\Delta\omega$ for the two tuning configurations in Fig. 2B. The gray band gives the region where Brillouin phase matching is possible, whereas the accessible $\Delta\omega$ range is shaded in orange. The plots show that Brillouin laser operation over the entire optical C-band is possible with a single device. This is demonstrated in Fig. 3B, where optical spectra show a series of pump and Brillouin laser operating wavelengths from a single device in which phase matching has been electrically controlled. In the spectra, the peak at the lower (higher) optical wavelength corresponds to the pump (Brillouin) laser. The Brillouin laser has been pumped using a tunable external cavity diode laser. However, as shown in Fig. 1D, direct pumping from a hybrid-integrated semiconductor laser is also possible.

Broadband group velocity dispersion (GVD) tuning for dark- and bright-pulse generation at an arbitrary pumping wavelength is also possible. GVD (excluding single-ring waveguide dispersion, as defined by $D_{2,c} \equiv D_2 - D_{2,o}$) is evaluated by fitting the dispersion curve with a third-order polynomial (Fig. 3C). The envelope of the dispersion curves sets a boundary of accessible anomalous and normal dispersion, which is indicated by the shaded area (see also the supplementary materials). Figure 3, D and E, presents a series of bright and dark soliton spectra that were obtained using a single device that has been directly pumped by using the setup

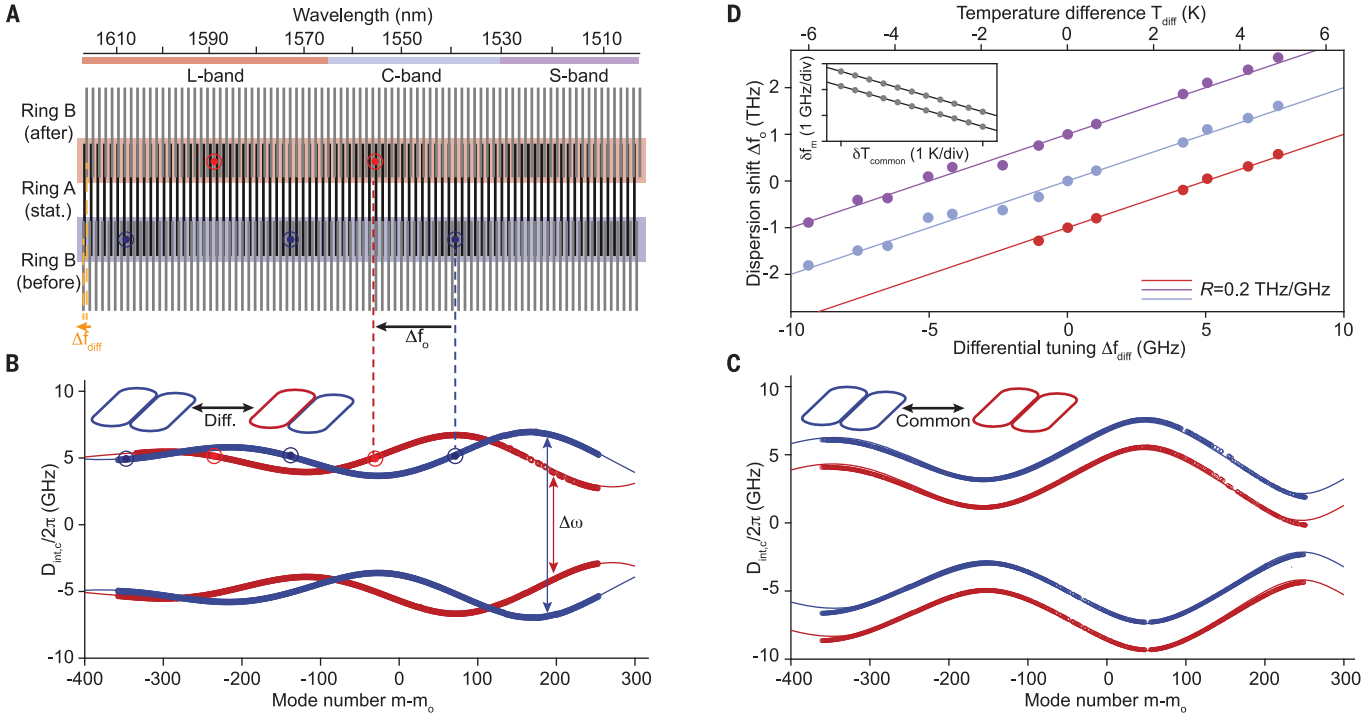

Fig. 2. Measurement of Moiré speedup of the dispersion spectrum. (**A**) Illustration of the Moiré pattern formed by mode frequencies in ring A and B resonators. A large shift Δf_o of the Moiré pattern is caused by a small uniform shift Δf_{diff} of the ring B frequencies. Brighter regions in the pattern correspond to degeneracy of the local ring modes and lead to strong modal hybridization. Here, ring A is assumed stationary (stat.), whereas ring B is tuned and illustrated before and after the differential tuning. (**B**) Each color shows the measured (bold) and fitted (fine solid line) dispersion spectra for the two frequency bands of the system plotted versus the relative mode number. Mode number m_o corresponds to 1550 nm. The red spectra result from differential heating. (**C**) Dispersion tuning for nondifferential heating (i.e., common-mode tuning) by 10 K (blue and red). No dispersion change is observed, and the curves have been intentionally offset by 2 GHz for comparison. (**D**) Measurement of the Moiré speedup effect wherein dispersion tuning of the circled dots in (A) are measured versus differential heating. Solid lines give a linear fit with Vernier ratio R = 0.2 THz/GHz. The three colors correspond to different reference points when evaluating the dispersion tuning, as illustrated in (A): S-band (light purple), C-band (light blue), and L-band (light red). The inset shows the calibration of mode-resonant-frequency shift versus chip temperature: $\delta f_o/\delta T_{common}$ = 1.561 ± 0.003 GHz/K (upper band) and 1.558 ± 0.001 GHz/K (lower band).

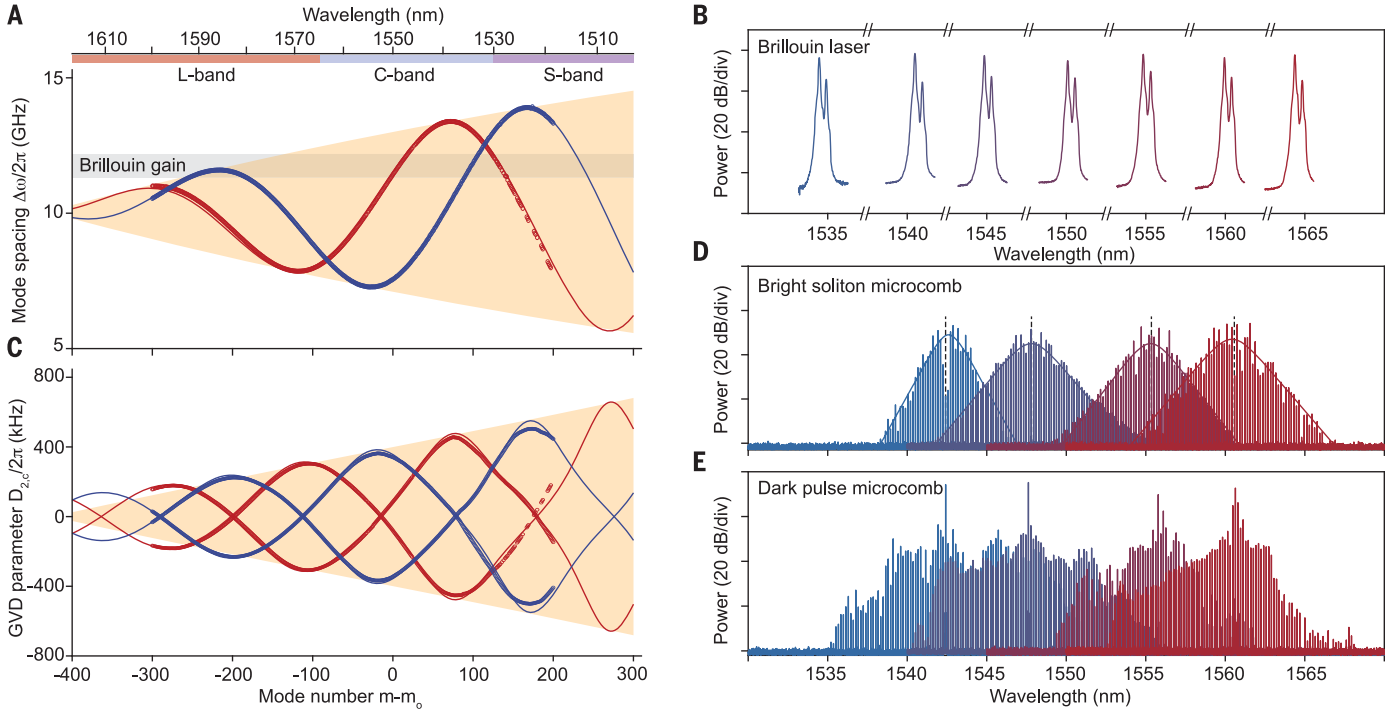

Fig. 3. Broadband operation of the Brillouin laser, bright-soliton microcomb, and dark-pulse microcomb. (**A**) Broadband tuning of the Brillouin phase-matching condition across the optical C-band and partial S- and L-bands. Frequency spacing between the upper and lower bands in Fig. 2 is plotted versus relative mode number (upper scale shows wavelength) for two different T_{diff}. Red and blue curves are data (bold curve) and model (fine curve). The orange region gives the accessible mode frequency spacing. The gray area indicates the approximate frequencies where Brillouin gain is possible. (**B**) Experimental demonstration of reconfigured Brillouin lasing across the optical C-band. (**C**) Reconfiguration of group velocity dispersion (GVD) for bright-soliton and dark-pulse generation. The fitted GVD parameter D_{2c} at two different T_{diff} is plotted versus relative mode number (upper scale shows wavelength). Red and blue curves are data fit (dots) and model (fine curve). The orange region gives the theoretically accessible D_{2c} values. The discontinuity of the red dots at large relative mode numbers is due to the insufficient bus-ring coupling at shorter wavelengths, which makes it challenging to capture and analyze these mode resonances. (**D** to **E**) Experimental demonstration of reconfigured bright-soliton microcomb (D) and dark-pulse microcomb (E) under DFB laser self-injection–locked operation at four different wavelengths. Mode locking is confirmed by the high signal-to-noise ratio photodetected repetition rate tone in fig. S3.

in Fig. 1B. We used four different distributed-feedback (DFB) semiconductor lasers operating at four different wavelengths. At each pumping wavelength, tuning of the resonator dispersion allows operation in either the bright or dark mode (*7*, *8*). A measurement of real-time switching between a bright-soliton and dark-pulse microcomb state is presented in fig. S4. As an aside, because there is no optical isolation or amplification of the pumping lasers in these measurements, the setup is suitable for integration and also operates in the self-injection locking (Turnkey) mode (*30*, *31*).

Conclusions

We demonstrate that a single microresonator device is electrically reconfigurable for operation as a Brillouin laser, a bright-soliton microcomb, or a dark-pulse microcomb. This capability allows identical devices from the same wafer to be used in very different applications or even mixed-mode operation on the same photonic chip. Consisting of a hybrid-integrated DFB laser (without optical isolators or amplifiers) and coupled-ring resonator, the module is capable of full heterogeneous integration (*32*). The dispersion reconfiguration is also compatible with microresonators with larger *FSR*s as well as faster actuators, including piezoelectric (*33*–*35*) and electro-optic control (*36*, *37*) when required. Other potential applications that may benefit from the enhanced tunability include resonant electro-optic frequency combs (*38*) and terahertz-wave generation (*39*, *40*).

REFERENCES AND NOTES

1. B. E. Little, S. T. Chu, H. A. Haus, J. Foresi, J.-P. Laine, *J. Lightwave Technol.* **15**, 998–1005 (1997).
2. J. C. Hulme, J. K. Doylend, J. E. Bowers, *Opt. Express* **21**, 19718–19722 (2013).
3. X. Xue *et al*., *Laser Photonics Rev.* **9**, L23 (2015).
4. Ó. B. Helgason *et al*., *Nat. Photonics* **15**, 305–310 (2021).
5. Y. Okawachi *et al*., *Opt. Lett.* **47**, 2234–2237 (2022).
6. Ó. B. Helgason *et al*., *Nat. Photonics* **17**, 992–999 (2023).
7. Q.-X. Ji *et al*., *Optica* **10**, 279 (2023).
8. Z. Yuan *et al*., arXiv:2301.10976 [physics.optics] (2023).
9. G. Oster, Y. Nishijima, *Sci. Am.* **208**, 54–63 (1963).
10. E. Gabrielyan, arXiv:physics/0703098 [physics.optics] (2007).
11. T. Herr *et al*., *Nat. Photonics* **8**, 145–152 (2014).
12. M.-G. Suh, K. J. Vahala, *Science* **359**, 884–887 (2018).
13. P. Trocha *et al*., *Science* **359**, 887–891 (2018).
14. M.-G. Suh, Q.-F. Yang, K. Y. Yang, X. Yi, K. J. Vahala, *Science* **354**, 600–603 (2016).
15. C. Bao *et al*., *Nat. Commun.* **12**, 6573 (2021).
16. D. T. Spencer *et al*., *Nature* **557**, 81–85 (2018).
17. Z. L. Newman *et al*., *Optica* **6**, 680 (2019).
18. M.-G. Suh *et al*., *Nat. Photonics* **13**, 25–30 (2019).
19. E. Obrzud *et al*., *Nat. Photonics* **13**, 31–35 (2019).
20. X. Xue *et al*., *Nat. Photonics* **9**, 594–600 (2015).
21. I. Kudelin *et al*., arXiv:2307.08937 [physics.optics] (2023).
22. A. Fülöp *et al*., *Nat. Commun.* **9**, 1598 (2018).
23. H. Shu *et al*., *Nature* **605**, 457–463 (2022).
24. J. Li, H. Lee, T. Chen, K. J. Vahala, *Opt. Express* **20**, 20170–20180 (2012).
25. S. Gundavarapu *et al*., *Nat. Photonics* **13**, 60–67 (2019).
26. H. Lee *et al*., *Nat. Commun.* **4**, 2468 (2013).
27. Y.-H. Lai *et al*., *Nat. Photonics* **14**, 345–349 (2020).
28. W. Loh *et al*., *Nature* **588**, 244–249 (2020).
29. J. Li, H. Lee, K. Y. Yang, K. J. Vahala, *Opt. Express* **20**, 26337–26344 (2012).
30. N. Pavlov *et al*., *Nat. Photonics* **12**, 694–698 (2018).
31. B. Shen *et al*., *Nature* **582**, 365–369 (2020).
32. C. Xiang *et al*., *Nature* **620**, 78–85 (2023).
33. W. Jin, R. G. Polcawich, P. A. Morton, J. E. Bowers, *Opt. Express* **26**, 3174–3187 (2018).
34. K. Alexander *et al*., *Nat. Commun.* **9**, 3444 (2018).
35. J. Liu *et al*., *Nature* **583**, 385–390 (2020).
36. C. Wang *et al*., *Nat. Commun.* **10**, 978 (2019).
37. Y. He *et al*., *Nat. Commun.* **14**, 3467 (2023).
38. M. Zhang *et al*., *Nature* **568**, 373–377 (2019).
39. D. Pidgayko *et al*., *Optica* **10**, 1582 (2023).
40. D. A. Chermoshentsev *et al*., *Opt. Express* **30**, 17094–17105 (2022).
41. Q.-X. Ji *et al*., Data. Figshare (2023); https://doi.org/10.6084/m9.figshare.24668871.v1.

ACKNOWLEDGMENTS

We thank H. Blauvelt at EMCORE Corporation for supplying the DFB lasers. **Funding:** This work was supported by the Defense Advanced Research Projects Agency (DARPA) (W911NF2310178 and HR0011-22-2-0009) and by the Air Force Office of Scientific Research (AFOSR) (FA9550-23-1-0587). **Author contributions:** The concepts were developed by Q.-X.J., P.L., W.J., J.E.B., and K.J.V. W.J. and J.G. designed and fabricated the device with assistance from L.W., Q.-X.J., J.P., A.F., and M.P. L.W. packaged the DFB lasers used in this study. Q.-X.J. and P.L. performed the measurements with assistance from Z.Y. All the authors analyzed the data and wrote the manuscript. K.J.V. and J.E.B. supervised the project. **Competing interests:** The authors declare no competing financial interests. **Data and materials availability:** All data are available in the manuscript, in the supplementary materials, or at Figshare (*41*). **License information:** Copyright © 2024 the authors, some rights reserved; exclusive licensee American Association for the Advancement of Science. No claim to original US government works. https://www.science.org/about/science-licenses-journal-article-reuse

SUPPLEMENTARY MATERIALS

science.org/doi/10.1126/science.adk9429
Materials and Methods
Figs. S1 to S4
References (*42*, *43*)
Movie S1

Submitted 20 September 2023; accepted 10 January 2024
10.1126/science.adk9429